

Carbon nanotubes as removable templates for metal oxide nanocomposites and nanostructures

P. M. Ajayan*, O. Stephan*, Ph. Redlich*† & C. Colliex*

* Laboratoire de Physique des Solides associé en CNRS, Université Paris-Sud, Bâtiment 510, 91405 Orsay, France
 † Max-Planck-Institut für Metallforschung, Institut für Werkstoffwissenschaft, Seestrasse 92, D-70174 Stuttgart, Germany

SEVERAL techniques have been developed recently for fabricating nanocomposite structures by filling^{1–3} carbon nanotubes^{4,5}. Here we show that surface-tension effects can induce the growth of uniform, thin metal oxide films—sometimes only a monolayer thick—on the outside of nanotubes, along with oxide fillings in the internal cavities and thin oxide layers between the concentric shells of the tubes. We report the preparation of such nanotube–oxide composites by annealing a mixture of partially oxidized nanotubes and V₂O₅ powder in air above the melting point of the oxide. The external coatings of the tubes are crystalline sheets of the V₂O₅ layer-like structure, which grow with the *c* axis parallel to that of the nanotube layers. Intercalation of the oxide occurs where there are missing shells in the nanotubes. We also show that the nanotubes can be partially removed by oxidation, leaving behind layered oxide fibres. Given the importance of vanadium oxides as catalysts and functional ceramics, this role of nanotubes as removable templates might lead to useful new kinds of nanostructured materials.

Carbon nanotubes produced by the arc-discharge method⁵ were ground and partially oxidized in air⁶ or nitric acid² to open some of the nanotube tips. The oxidized sample was then mixed and ground with pure V₂O₅ powder (dark orange) in approximately 1:1 weight ratio. The mixture was heated in an oven in air at ~750 °C (melting point of the oxide is 690 °C) for ~20 minutes. The annealed mixture (black) was crushed, dispersed in ethanol and observed by transmission electron microscopy (TEM) (Topcon 0020B) and scanning transmission electron microscopy (STEM) (VG HB 501).

We found that a large fraction of the open nanotubes were filled with the oxide. The fillings have diameters as small as 1–2 nm and extend continuously over several hundred nanometres. In cavities smaller than ~3 nm, the filling has an amorphous

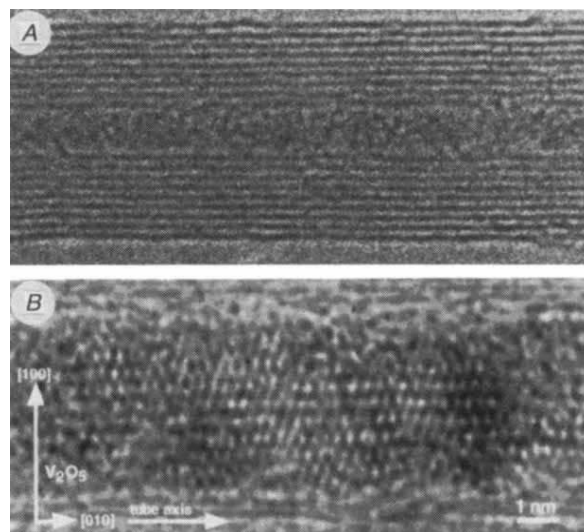


FIG. 1 High-resolution TEM images of tubes filled (darker contrast in the centre) with vanadium oxide. A, Filling in a narrow internal hollow, showing amorphous structure. B, Crystalline V₂O₅ structure in a larger hollow (only 2–3 tube layers around the filling is shown) showing preferred orientation with respect to the tube axis.

structure and the contrast in the images suggests that it has high porosity (Fig. 1A). In larger cavities however, the filled phase corresponds to crystalline V₂O₅, and in some cases the structure clearly exhibits a preferred orientational relationship with the tube axis (Fig. 1B; the *b* axis of V₂O₅ is parallel to the tube axis), suggesting directional solidification of the molten oxide in the cavity. This striking change in solidification behaviour as the cavity size is reduced (stabilization of amorphous phase; also see ref. 1) is in agreement with recent theoretical predictions⁷ of filling with lead. From capillarity studies of nanotubes⁸, a surface tension of less than 100–200 mN m⁻¹ is needed for any material to wet (and fill) nanotube surfaces. Molten V₂O₅ has extremely low surface tension (~80 mN m⁻¹, comparable to water which has a value of ~72 mN m⁻¹)⁹ and should strongly wet nanotubes. In fact, the only pure binary oxides that satisfy the above wetting criteria are PbO, Bi₂O₃, V₂O₅, WO₃, MoO₃ and B₂O₃; the first three have all been reported to fill nanotubes by capillarity (refs 1, 6 and this work).

As well as observing capillarity-induced filling of nanotubes, we find many isolated nanotubes covered (also by capillarity)

FIG. 2 Images of oxide-filling/nanotube/oxide-coating sandwich structures. *a*, Lower-magnification image showing uniform coatings on the left (completely covered for more than a few hundred nanometres) and right parts of the tube, with no coating in the centre. Filling is also seen inside the tube. *b*, Image at higher magnification resolving the 0.34-nm (002) fringes of the carbon nanotube. Coatings of oxide, uniform in thickness, can be seen on the upper and lower parts of the tube. The cylindrical profile of the coating is seen on the right side of the image. A diagram of capillarity-induced filling and coating of open tubes is shown at the bottom of the figure.

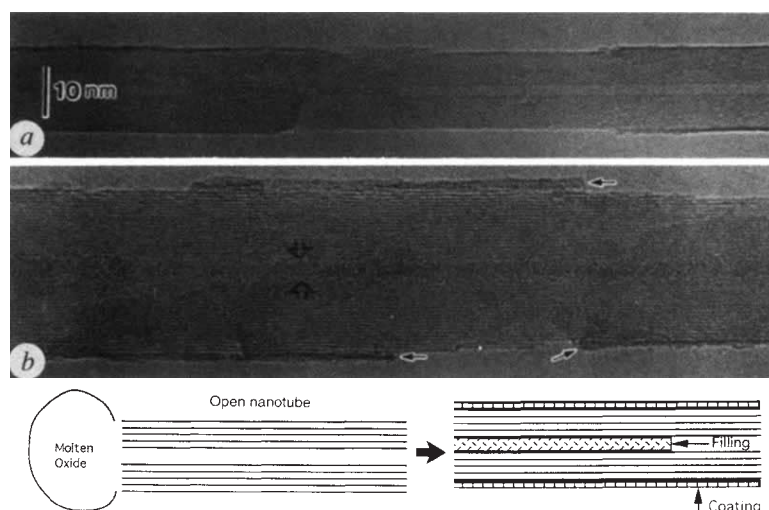
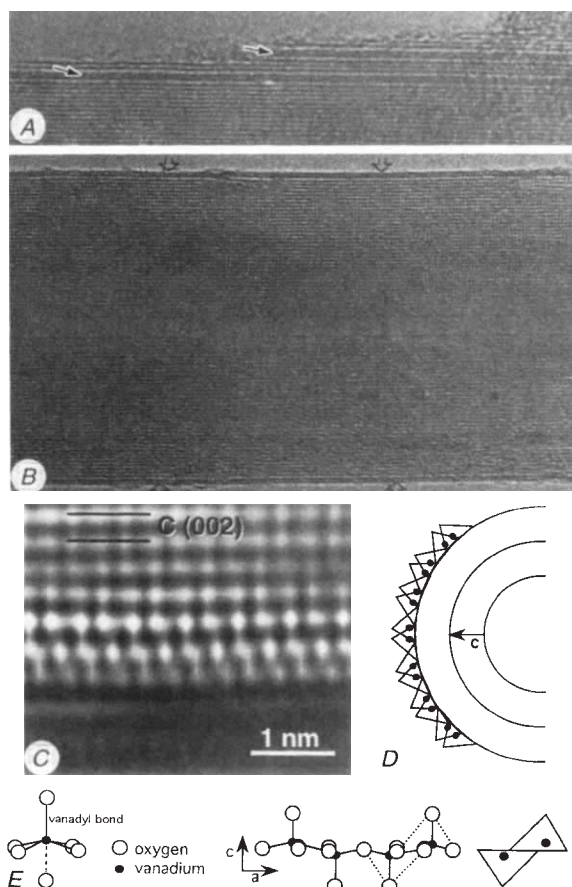
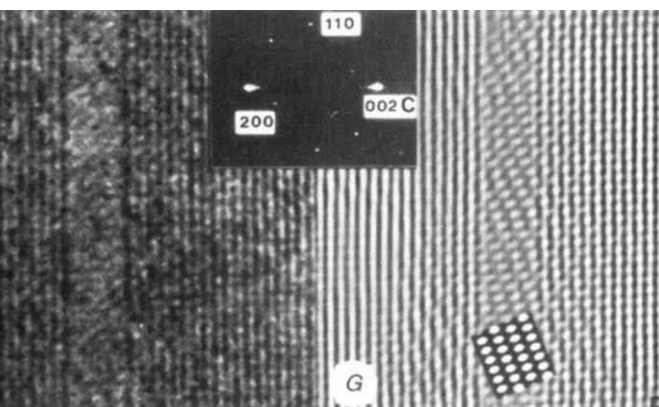


FIG. 3 High-resolution TEM images of nanotubes after heating with V_2O_5 at 750 °C. A, Intercalation by V_2O_5 in the gaps where nanotube layers are missing (arrows). Only a few outer fringes of a larger tube are shown. B, Cross fringes in the nanotube image, arising from the interference between (002) planes of graphite (0.34 nm) and V_2O_5 lattice in [001] projection. C, Higher-magnification image of the fringe structure due to the oxide coating at the edge of the tube shown in B (arrows). The image is Fourier filtered. D, Diagram showing the arrangement of structural pyramid units on the surface of the tube, viewed parallel to the tube axis. The outermost circle drawn does not represent a nanotube shell. The arrow indicates the direction of the *c* axis in the nanotube. In this case, the V_2O_5 layer is projected in the [110] direction. E, Diagram of a basic pyramidal unit of V_2O_5 and a projection of a monolayer onto the *b* plane, showing upward and downward pointing pyramids. In D triangles representing pyramids point only outwards, because we assume that the inner vanadyl oxygens are missing. F, Analysis of the projected image of a coated tube acquired using a slow-scan CCD camera. The Bragg filtered diffractogram (inset) shows the superposition of the (002) spots (labelled 'C') from the carbon tube and the (110) and (200) spots corresponding to the overlayer V_2O_5 . The image is reconstructed in G by use of these spots. The contrast due to the oxide is clearly visible in the central hollow region. It matches well with a simulated image (inserted in G) of one monolayer of V_2O_5 in [001] projection at the optimum defocus (Scherzer) condition for phase-contrast imaging.



with extremely thin films of the oxide. In the sample, we also observe nanotube bundles covered with thicker deposits of the oxide. Figure 2 shows 'sandwich' structures of individual nanotubes which have inner fillings and thin outer oxide coverings. The coatings on isolated nanotubes are uniform in thickness and are rarely observed to be thicker than 1 nm. The coatings do not always cover the entire nanotube surface but continuous cylindrical films are seen to extend for lengths up to a few hundred nanometres. Commonly, films are not observed on the surfaces of very small tubes (<5 nm) nor on the tips of nanotubes and nanoparticles.

We often observe intercalation of V_2O_5 in the gaps (as small as twice the tube layer spacing) left by partially missing shells (owing to scroll-like defects¹⁰ or removed during oxidation) (Fig. 3A). No inter-tube-layer expansion is seen, as the adjacent cylindrical layers are fixed. Figure 3B shows a typical high-resolution TEM image from a larger tube coated with monolayer film. The image shows cross fringes arising from the interference between the pseudolattice from the carbon nanotube (002) layers and the overlying oxide lattice. The outermost fringe in the image corresponds to the oxide film coating (Fig. 3C) and represents the projection from the curved V_2O_5 layer (built from VO_5 pyramidal structural units sharing edges and corners (Fig. 3E))^{11,12} decorating the tube surface (see Fig. 3D). V_2O_5 has a layer-like structure, with the layers held together by weak V–O (vanadyl, 0.28-nm) bonds. We suggest that in the monolayer film only outward-pointing pyramids exist, leading to vanadyl oxygen vacancies, which has been observed for V_2O_5 surfaces^{11–14}. The missing vanadyl oxygens (discussed later) would give greater freedom for the layers to bend¹¹ and would allow a better match between the pyramidal bases of the V_2O_5 and the carbon lattice (see the epitaxial relation described later). For the intercalated films, this leads to the possibility of flat basal planes with no vanadyl oxygens sticking out of the



plane. Because of the tilt of the tube with respect to the imaging direction¹⁵ or actual bending of planes in the film, we often observe fringes due to the film curving around the tube axis.

To understand the symmetry and orientation of the coated film on nanotubes and to minimize radiation damage in the oxide layer, images from tubes with monolayer coatings (Fig. 3F) were acquired using a slow-scan CCD (charge-coupled device) camera. The Fourier transform of the image (inset) shows (002) spots of the nanotube along with spots corresponding to (200) and (110) planes of V_2O_5 , which has an orthorhombic unit cell¹¹, in the [001] (*c*-axis) projection. The relative interplanar distances and angles are correct within an error of 5% which could be due to distortions in the curved lattice. The contrast seen in the area corresponding to the central nanotube hollow of the Bragg filtered image (Fig. 3G) compares well with a simulated image (inserted in Fig. 3G) of one layer of V_2O_5 . The missing vanadyl oxygens in the structure do not alter the

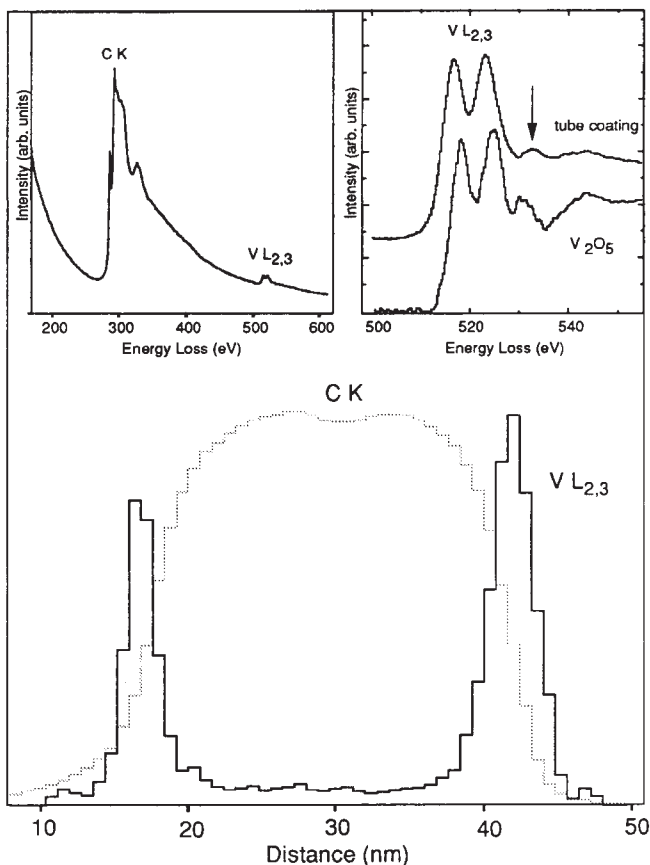


FIG. 4 Electron energy-loss spectra from coated nanotubes. Core loss spectra showing graphite (K) edge due to the nanotube and the vanadium (L) edge due to the coating (left inset). The oxygen (L) edge at 532 eV is superimposed on the V L-edge. The fine structure (right inset) of the oxide L-edge suggests oxygen deficiency in the V_2O_5 coated films (for comparison, fine structure from bulk V_2O_5 taken using the same scan interval (0.2–0.8 s) is shown). The energy width between the L-edges and the oxygen prepeak (arrow) is larger for the coated film (typical signature for oxygen loss) and the $L_{2,3}$ peaks look symmetrical compared to that from pure V_2O_5 . The main figure shows intensity profiles calculated from line spectra across a 25-nm tube for the V L-edge and C K-edge. The profiles indicate the presence of a thin layer of vanadium around the surface of a large nanotube with a small hollow.

image contrast in this projection. The result suggests that during melting, wetting and solidification of the oxide on nanotubes, individual sheets have topotactically grown on the tube surfaces with their c axis normal to the curved graphite layers.

The layered nature of the oxide seems to help in obtaining such fine and uniform coatings because individual sheets slide easily with respect to each other. During intercalation of V_2O_5 , the layers can buckle¹² where the pyramidal units share only corners, suggesting that the sheets could effectively bend to cover the nanotubes. On the smallest tube on which coating was observed (~ 5 nm), this corresponds to 8.2° bending between pyramids, and 44 such pyramids are needed to cover one tube circumference if the film has its a axis parallel to the tube axis. After analysing many images of tubes with coated films, we fail to see any preferential orientation of the a and b axes of the V_2O_5 sheets with respect to the tube axis, although there could be orientational alignment between the film and the substrate lattices. It is impossible at this stage to assess this relationship because the helicity of sheets of carbon atoms⁴ in the outer layer of a multilayer tube cannot be uniquely determined.

The existence of oxygen vacancies in the film, such as missing vanadyl oxygens, is consistent with our results from electron

energy-loss spectroscopy (EELS) and observations^{13,14} on V_2O_5 indicating the formation of vanadyl surface defects after heat treatment. Spatially resolved line scans collecting electron energy-loss spectra¹⁶ across coated tubes (Fig. 4) gives concentration profiles indicating surface layers of vanadium oxide around carbon tubes. EELS from coated and filled tubes give signals corresponding to graphite and vanadium oxide¹⁷. For the vanadium L-edge, fine structure (Fig. 4 inset) is characteristic of oxygen-deficient stoichiometry compared to pure V_2O_5 . However, the reduced dimensionality of the oxide and radiation-induced oxygen loss^{18,19} may also contribute; but to minimize the latter we use very small scanning time intervals (see Fig. 4 legend).

As carbon nanotubes oxidize below the melting point of V_2O_5 (ref. 6), we attempted to see if the nanotubes can be preferentially removed by oxidation to leave behind some of the coated films and fillings. A second oxidation run at 650–675 °C in air was carried out on the annealed sample for ~ 45 minutes, until the sample turned orange-grey (close to V_2O_5 colour) and the

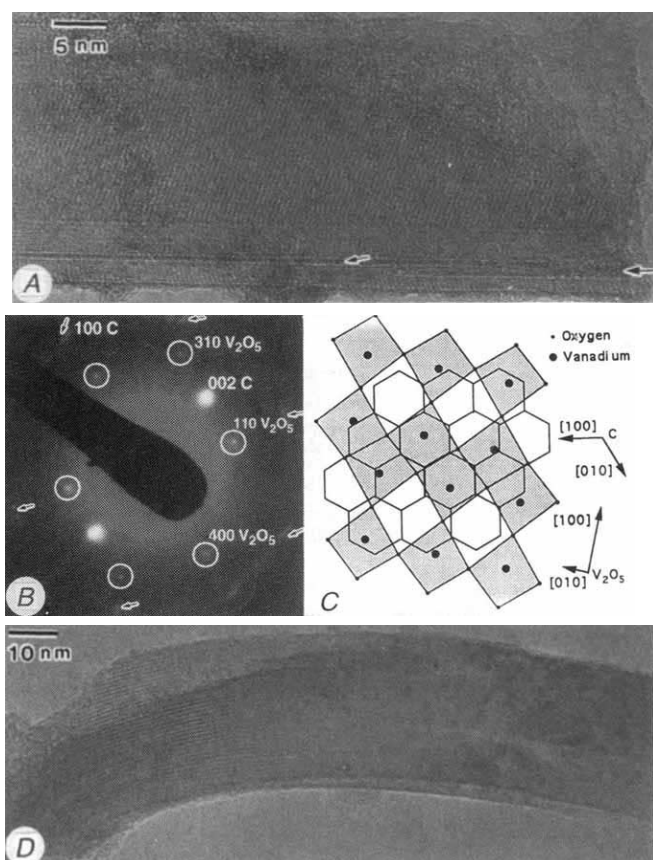


FIG. 5 Images from twice-oxidized sample (see text) showing the selective removal of carbon nanotube templates. A, Tip of a coated tube showing etching of the nanotube layers from the inside out. The coated film is seen near the open tube end (top right in the image) where the carbon tube has burnt away. Typical fringe contrast due to the outer oxide film is clearly visible because of the expanded tube hollow. The initial size of the hollow in this tube was only ~ 4 nm (seen away from the tip, but not shown in this image). Intercalation by the oxide is also seen in this tube (indicated by arrows). B, Electron diffraction pattern taken from the upper part of tip region of this tube (digitized and contrast-enhanced pattern). Faint spots due to V_2O_5 are marked with circles. Only the inner circle of $(hk0)$ spots is shown (indicated by arrows). C, Superposition of the distorted square net of the oxide lattice and the graphite hexagons, corresponding to the electron diffraction pattern in B. D, Image of a fibrillar structure of pure V_2O_5 left behind after the supporting nanotube has been removed. The structure is partially bent because of electron irradiation.

sample quantity reduced by about half. Among the few nanotubes left behind in this twice-oxidized sample, the ratio of coated to uncoated tubes had increased dramatically (>80%). Observation of the tips of the remaining coated tubes showed that, in most cases, oxidation has preferentially etched the inner layers of the tube, leaving the outer coatings and few outer tube layers (Fig. 5A) and giving clearer views of the coated film through the enlarged tube centres. This contrasts with the oxidation behaviour of pure nanotubes, where the attack proceeds from the outside to the inside, leaving chisel-shaped tips.

A possible orientational relationship between the outermost tube-layer lattice and the coated film now becomes discernible in some cases (using electron diffraction; Fig. 5B), owing to the selective removal of most of the inner layers. The few remaining outer tube layers (Fig. 5A) produce a narrow angular spread for the (*hk*0) spots ($\sim 4^\circ$), and the approximate orientation of the outer carbon honeycomb lattice can be determined with respect to the tube axis. The orientation of the oxide lattice can be deduced from the visible V_2O_5 spots in the diffraction pattern. In this case the (001) V_2O_5 basal planes grow on the (001) graphite surface with a near-parallel coincidence for two sets of planes; the (100) graphite|| (110) V_2O_5 , and (010) graphite|| (310) V_2O_5 (Fig. 5B, C). For the second set of planes the spacing mismatch ($\sim 20\%$) is in the range that could introduce van der Waals epitaxy^{20,21} in the system, as observed in layered dichalcogenides and Langmuir–Blodgett films. This type of lattice alignment occurs between weakly interacting surfaces with no dangling bonds (on cleavage planes, as here).

After the second oxidation, we find that the sample contains mainly larger (micrometre-sized) oxide structures, which covered nanotube bundles initially but now show pure oxide composition and hollow morphology (from EELS mapping), all graphitic structures having been removed. There are many extremely thin oxide skins (typically 10–50 nm in width, up to few hundred nanometres long and <1 nm thick) left behind in the sample. We see a few cylindrical structures of dimensions typical of larger nanotubes (Fig. 5D) of pure V_2O_5 (verified by diffraction and EELS). The observed skins could have originated from discontinuous films on nanotubes or from continuous films broken during sonication. The nanofibrils of V_2O_5 are flexible and collapsible under electron irradiation. We also find some solid rod-like V_2O_5 structures with a morphology typical of the filling in tubes, typically 5–8 nm in diameter and a few hundred nanometres long. The results indicate that nanotube templates are partially removable and point to their possible use as degradable templates to fabricate new ceramic films having layered structures.

The ability to coat the unreactive graphite basal planes that make nanotube surfaces with thin V_2O_5 films increases the versatility of nanotubes, because V_2O_5 is a good building block for catalytic complexes by organic routes²². Coated conventional carbon fibres have found a variety of applications²³. Coated and filled nanotube sandwich structures should have vastly different optical and electrical properties, and have better oxidation resistance (from our observations) than pure nanotubes. Vanadium pentoxide is an important catalyst²⁴ and a functional ceramic with uses ranging from batteries to switching elements^{25,26} with properties depending closely on dimensionality and oxygen stoichiometry. There is a great industrial interest in growing thin films of different vanadium oxides²⁷. Our results point to a new synthesis route for the fabrication of such thin-film ceramic nanostructures using nanotubes as efficient templates. □

Received 20 April; accepted 22 May 1995.

1. Ajayan, P. M. & Iijima, S. *Nature* **361**, 333–334 (1993).
2. Tsang, S. C., Chen, Y. K., Harris, P. J. F. & Green, M. L. H. *Nature* **372**, 159–162 (1994).
3. Guerret-Piécourt, C., Le Bouar, Y., Loiseau, A. & Pascard, H. *Nature* **372**, 761–765 (1994).
4. Iijima, S. *Nature* **354**, 56–58 (1991).
5. Ebbesen, T. W. & Ajayan, P. M. *Nature* **358**, 220–222 (1992).
6. Ajayan, P. M. et al. *Nature* **362**, 522–525 (1993).
7. Prasad, R. & Lele, S. *Phil. Mag. Lett.* **70**, 357–361 (1994).

8. Dujardin, E., Ebbesen, T. W., Hiura, H. & Tanigaki, K. *Science* **265**, 1850–1852 (1994).
9. Ikemiyama, N., Umemoto, J., Hara, S. & Ogino, K. *ISIJ Int.* **33**, 156–165 (1993).
10. Amelinckx, S. et al. *Science* **267**, 1334–1338 (1995).
11. Galy, J. J. *Solid St. Chem.* **100**, 229–245 (1992).
12. Cava, R. J. et al. *J. Solid St. Chem.* **65**, 63–71 (1986).
13. Oshio, T., Sakai, Y. & Ehara, S. *J. Vac. Sci. Technol.* **B12**, 2055–2059 (1994).
14. Smith, R. L., Lu, W. & Rohrer, S. *Surf. Sci.* **322**, 293–300 (1995).
15. Cullen, S. L., Boothroyd, C. B. & Humphreys, C. J. *Ultramicroscopy* **56**, 127–134 (1994).
16. Ajayan, P. M. et al. *Phys. Rev. Lett.* **72**, 1722–1725 (1994).
17. Lin, X. W. et al. *Phys. Rev.* **B47**, 3477–3481 (1993).
18. Smith, D. J., McCartney, M. R. & Bursill, L. A. *Ultramicroscopy* **23**, 299–304 (1987).
19. Fan, H. J. & Marks, L. D. *Ultramicroscopy* **31**, 357–364 (1989).
20. Zasadzinski, J. A. et al. *Science* **263**, 1726–1733 (1994).
21. Ohuchi, F. S., Parkinson, B. A., Ueno, K. & Koma, A. *J. appl. Phys.* **68**, 2168–2175 (1990).
22. Gai, P. L. & Kourtakis, K. *Science* **267**, 661–664 (1994).
23. Dresselhaus, M. S. et al. *Graphite Fibers and Filaments* (ed. Cardona, M.) 238–243 (Springer, Berlin, 1988).
24. Krylov, O. V. *Catalysis by Nonmetals* (ed. Loebel, E. M.) (Academic, New York, 1970).
25. Scarmínio, J. et al. *Electrochim. Acta* **38**, 1637–1642 (1993).
26. Kim, D. H. & Kwok, H. S. *Appl. Phys. Lett.* **65**, 3189–3191 (1994).
27. Shimizu, Y., Nagase, K., Miura, N. & Yamazoe, N. *Jap. J. appl. Phys.* **29**, L1708–L1711 (1990).

ACKNOWLEDGEMENTS. We thank P. Ballongue and C. Jeanguillaume for their help. P.R. acknowledges a grant from the DAAD (HSP-II).

Deflation of Mount Etna monitored by spaceborne radar interferometry

Didier Massonnet*, Pierre Briole† & Alain Arnaud‡

* Centre National d'Etudes Spatiales, 18 Avenue E. Belin, 31055 Toulouse, France

† Institut de Physique du Globe, 4 Place Jussieu, 75005 Paris, France

‡ Groupe CISI, 1 Rue des Cosmonautes, 31400 Toulouse, France

GROUND-BASED measurements of volcano deformation can be used to assess eruptive hazard, but require the costly (and often hazardous) installation and maintenance of an instrument network. Here we show that spaceborne radar interferometry, which has already shown its utility in mapping earthquake-related deformation¹, can be used to monitor long-term volcano deformation. Two families of synthetic aperture radar images, acquired from ascending and descending orbits by the satellite ERS-1, and looking at Mount Etna from opposite sides, cover the time period from 17 May 1992 to 24 October 1993, and include the second half of Etna's most recent eruption. Despite artefacts of the interferometric technique, we can observe a volcano-wide deflation, which is an expected consequence of the eruption, but which had not previously been appreciated. We quantify it using a simple model based on the change of pressure in a sphere located in an elastic half-space; the modelled deformation increases linearly with time until the end of the eruption. Our results show that it will be possible to use this technique to detect the inflation of volcanic edifices that usually precedes eruptions.

Mount Etna (Fig. 1) is one of the most active and best studied volcanoes in the world. The last eruption started on 14 December 1991 in the Valle del Bove, a large amphitheatre formed by collapse of the eastern flank. Lava was erupted along a fracture system that had opened in 1989², and covered most of the southern part of the Valle del Bove. The eruption stopped on 31 March 1993 after 473 days. The rate of lava production remained stable during most of the eruption, and the total erupted volume was $\sim 3 \times 10^8 \text{ m}^3$ (ref. 3).

To measure the deformation, we constructed interference patterns from the difference of pairs of synthetic aperture radar (SAR) images acquired by the ERS-1 satellite. This geodetic technique can measure centimetre-size changes in the ground surface^{1,4,6}. The resulting interferogram is a contour map of the change in range to the volcano surface, measured along the